



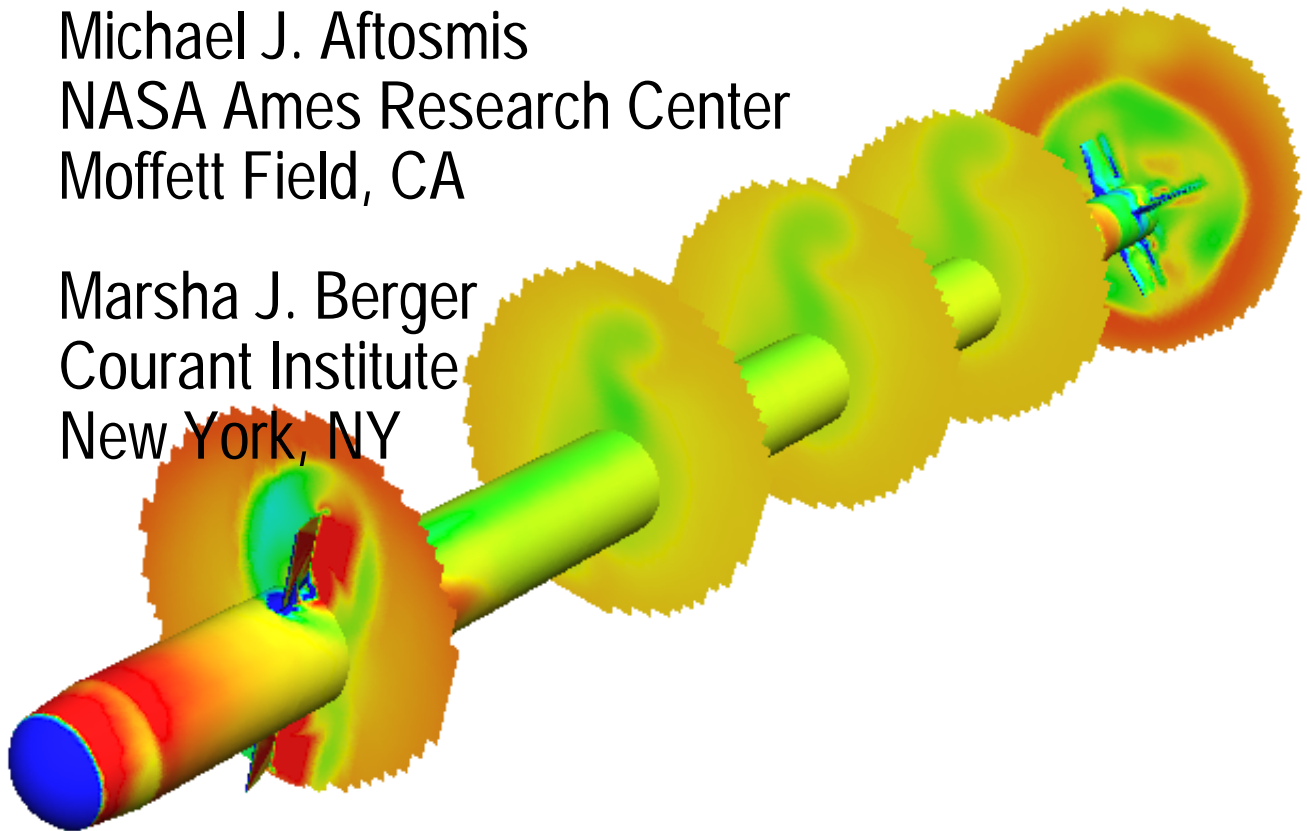
**AIAA-2002-2798**

**Numerical Simulation of Rolling-Airframes  
Using a Multi-Level Cartesian Method**

Scott M. Murman  
ELORET  
Moffett Field, CA

Michael J. Aftosmis  
NASA Ames Research Center  
Moffett Field, CA

Marsha J. Berger  
Courant Institute  
New York, NY



**20th AIAA Applied Aerodynamics Conference**

June 24-26, 2002 / St. Louis, MO

# Numerical Simulation of Rolling-Airframes Using a Multi-Level Cartesian Method

Scott M. Murman  
ELORET  
Moffett Field, CA 94035  
smurman@nas.nasa.gov

Michael J. Aftosmis  
NASA Ames Research Center  
MS T27B Moffett Field, CA 94035

Marsha J. Berger  
Courant Institute  
251 Mercer St.  
New York, NY 10012

## Abstract

A supersonic rolling missile with two synchronous canard control surfaces is analyzed using an automated, inviscid, Cartesian method. Sequential-static and time-dependent dynamic simulations of the complete motion are computed for canard dither schedules for level flight, pitch, and yaw maneuvers. The dynamic simulations are compared directly against both high-resolution viscous simulations and relevant experimental data, and are also utilized to compute dynamic stability derivatives. The results show that both the body roll rate and canard dither motion influence the roll-averaged forces and moments on the body. At the relatively low roll rates analyzed in the current work these dynamic effects are modest, however the dynamic computations are effective in predicting the dynamic stability derivatives which can be significant for highly-maneuverable missiles.

## 1 Introduction

The use of Computational Fluid Dynamics (CFD) to simulate the steady flow about static geometries is now common practice for engineers and analysts. The ability to routinely simulate dynamic configurations, where the geometry moves in some manner *during* a computation, however, is still a computationally-intensive problem. For many applications, such as rotorcraft, turbines, or rolling missiles, the motion of the body is a fundamental aspect of the simu-

lation and must be accounted for in some manner. The current work demonstrates an inviscid Cartesian method for simulating a rolling airframe with movable canard control surfaces. The Cartesian method provides an efficient, automated, and robust approach for performing CFD simulations about arbitrarily complex geometries (cf. Refs. [1, 2]).

There are several numerical schemes capable of simulating a dynamic configuration where active control surfaces move relative to the body (cf. Refs. [3, 4, 5, 6]), however few methods have been applied to the analysis of a rolling airframe. Weinacht et al. [7, 8], demonstrated methods for analyzing axisymmetric geometries with fins, using steady-state algorithms to determine the pitch-damping coefficient. Recently, Oktay and Akay [9] and Park et al. [10], performed unsteady dynamic simulations of a simple finned missile geometry using rigid domain motions in order to compute a general set of dynamic stability derivatives. Janus et al. [11] demonstrated a multi-block structured approach for relative body motion on a prop-fan cruise missile, and recently Hall [12] applied an overset structured approach to the simulation of a rolling airframe with dithering canards.

The current work presents a general method for simulating moving geometries with relative body motion in 3D. This method is applied to the simulation of a rolling missile with both fixed and moving canard control surfaces. An efficient scheme for computing dynamic stability derivatives using rigid domain motions is presented and utilized to compute the damping coefficients for the current missile configuration. Comparisons are made for the current results between static and dynamic simulations, against high-fidelity viscous simulations [13], and also against relevant experimental data [14].

---

Copyright ©2002 by the American Institute of Aeronautics and Astronautics, Inc. No copyright is asserted in the United States under Title 17, U. S. Code. The U. S. Government has a royalty-free license to exercise all rights under the copyright claimed herein for Governmental purposes. All other rights are reserved by the copyright owner.

## 2 Numerical Method

### 2.1 Geometry and Computational Mesh

The canard-controlled missile considered in this work is shown in Fig. 1 for its zero-roll ( $\phi = 0^\circ$ ) configuration. The canards are shown in their zero-deflection position. The body is approximately shaped like a hemisphere-cylinder and has a fineness ratio (length/diameter) of roughly 20. There are four fixed, interdigitated tails which are canted  $1^\circ$  to generate a counter-clockwise roll when viewed from the nose, and two canards which act as control surfaces. These canards are interconnected so that their motion is synchronous, and as the body rolls the canards can change positions to affect controlled movements, such as yaw or pitch. This canard motion is sometimes referred to as “dithering”. Two canard dither schedules based on an analytic model of Stalnaker [15] are considered in this work, and they are both outlined in Fig. 2 for a body roll rate of 8.75 Hz (positive roll is counter-clockwise when viewed from the nose). The canards can sustain only two positions; either the minimum or maximum deflection angle, which is  $\pm 15^\circ$  in this case. As the body rolls, the canards dither between their min. and max. deflection angles at discrete roll positions. For example, in Dither Schedule 0 the canards start to move from  $-15^\circ$  deflection at  $\phi = 0^\circ$ . The time of travel between the two deflection angles corresponds to approximately 21 degrees of roll at this roll rate, so that at  $\phi = 21^\circ$  the canards are positioned at  $+15^\circ$  deflection. It’s also possible that the canards do not complete their travel before being instructed to “reverse”, as can be seen in Dither Schedule 1 near  $\phi = 200^\circ$ . Note that both of the canard dither schedules are periodic over one complete revolution of the body.

The current configuration poses a challenge, especially when creating a computational mesh which can be solved efficiently, due to the large variation in physical scales which must be resolved. The sharp edges of the canards must be resolved in order to generate strong canard tip vortices. These canard vortices must be preserved as they convect the length of the body in order to resolve the canard vortex/tail interaction that occurs at low-moderate angles of attack. Further, the large bow shock that forms ahead of the body in supersonic flow, as well as the shock structures around the canards and fins, must also be resolved. Volume mesh generation was performed using the Cartesian meshing scheme of Aftosmis et al. [1]. This package takes as input the triangulated surface geometry and generates an unstructured Cartesian volume mesh by subdividing the computational domain based upon the geometry. In this manner, the sharp geometric features contain refined

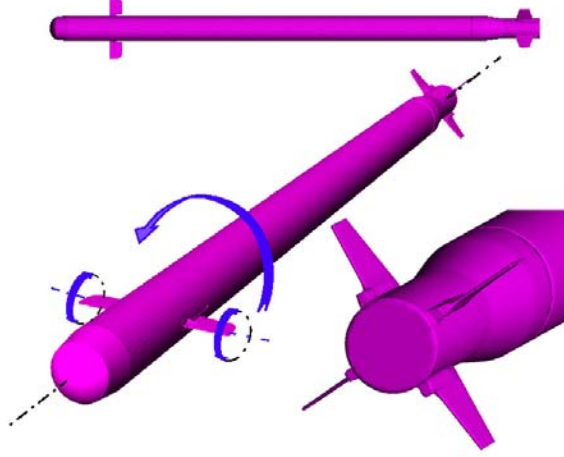


Figure 1: Missile surface geometry.

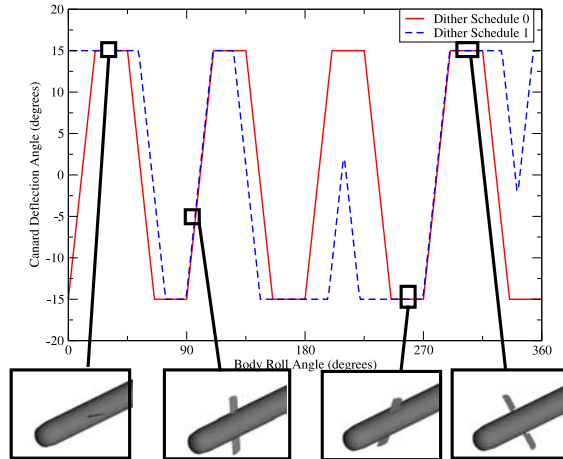


Figure 2: Motion of canard control surfaces for 8.75 Hz body roll rate.

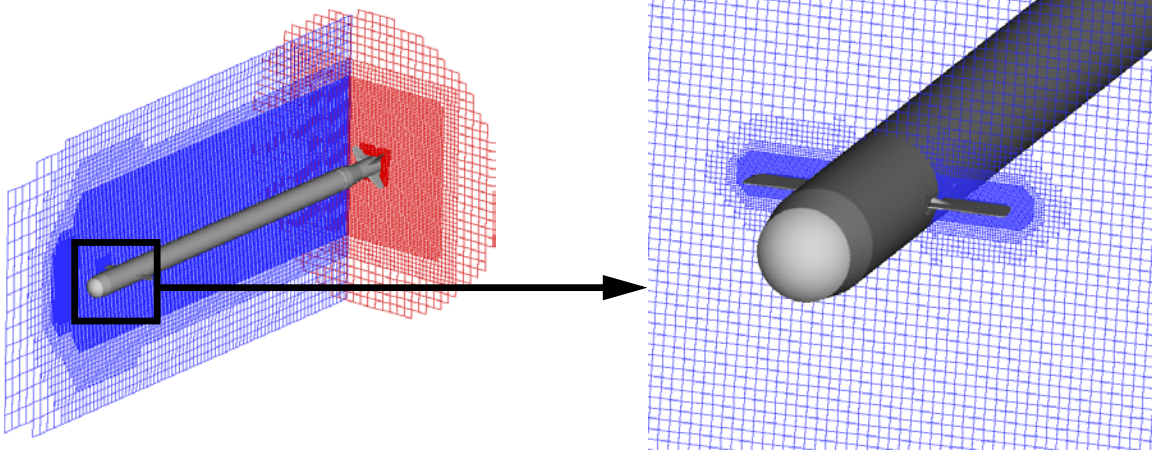


Figure 3: Cutting planes through Cartesian mesh.

cells, while areas away from the geometry maintain a relatively coarse spacing. The intersection of the solid geometry with the regular Cartesian hexahedra is computed, and polyhedral cells are formed which contain the embedded boundary. Cells in regions interior to the solid geometry are removed. The solid-wall boundary conditions for the flow solver are then specified within these “cut-cell” polyhedra. The volume meshing procedure is provably robust, and does not require user intervention (cf. Refs. [1,16] for more details on the Cartesian volume meshing). Optionally, volume regions within the domain can be specified to contain a specific resolution. These pre-specified regions are utilized in the current work to resolve the bow shock ahead of the body, and the canard vortex trajectory on the leeward side of the fuselage. Fig. 3 shows a lateral cutting plane through the canard, as well as two axial cutting planes along the body; one just behind the canards, and one intersecting the tail section. The resolved regions for the shocks and the uniform vortex region the length of the body are clearly visible, as well as the refinement near the sharp features of the geometry, such as the leading and trailing edges of the canards, and the tips of the tail fins.

A grid resolution study was performed using a static missile configuration at flow conditions  $M_\infty = 1.6$ ,  $\alpha = 3.0^\circ$ ,  $\phi = 0.0^\circ$ , and with the canards undeflected. These flow conditions represent a nominal baseline configuration for the current work, while the undeflected canards still generate strong vortices which impact the tail section. Simulations were performed using three mesh densities;  $1.2 \times 10^6$ ,  $3.4 \times 10^6$ , and  $6.0 \times 10^6$  cells. Computed results were compared in terms of the axial and normal forces, and pitching and rolling moments on the body. The difference between the medium and finest grids in terms of the integrated quantities was less than 3%. Com-

parison with highly-refined viscous simulations of Nygaard and Meakin [13] also showed results consistent with the difference between inviscid and viscous simulations. Based upon these findings, a grid density of roughly  $3.4 \times 10^6$  cells was utilized for all of the simulations, and this is the level of refinement shown in Fig. 3.

## 2.2 Cartesian Moving-Body Flow Solver

In order to simulate a rolling missile with dithering canards, it’s necessary to utilize a scheme that can allow rigid bodies to move relative to each other during a simulation. A general numerical scheme for solving time-dependent flows with (optional) rigid-body motion for unstructured Cartesian meshes was developed from the parallel, steady-state solver of Aftosmis et al. [2]. This section will provide a brief overview of the scheme. Complete details and analysis of the numerical scheme will be provided in a future publication [17].

### 2.2.1 Dual-time formulation

In order to leverage the infrastructure of the steady-state flow solver outlined in Ref. [2], a dual-time formulation (cf. Refs. [18,19]) was developed for the time-dependent scheme,

$$\begin{aligned} \frac{d\mathbf{Q}}{d\tau} + R^*(\mathbf{Q}) &= 0 \\ R^*(\mathbf{Q}) &= \frac{\partial \mathbf{Q}}{\partial t} + R(\mathbf{Q}) \end{aligned} \quad (1)$$

where  $\tau$  is referred to here as “pseudo-time”, and is the iterative parameter, and  $t$  is the physical time.  $\mathbf{Q}$  is the vector of conserved variables, and  $R(\mathbf{Q})$  is an appropriate numerical quadrature of

the flux divergence,  $\frac{1}{V} \oint_S \mathbf{f} \cdot \mathbf{n} dS$ . As  $\frac{d\mathbf{Q}}{d\tau} \rightarrow 0$  the time-dependent formulation is recovered. The multi-grid solver described in [2] is utilized to efficiently converge the inner pseudo-time integration. An explicit, multi-stage, pseudo-time-integration scheme is utilized to converge the “inner loop” in Eqn. 1. This is similar to the scheme outlined by Jameson [20], however, the semi-implicit approach of Melson et al. [21] is used here for the physical time-derivative term.

Various time-dependent schemes can be constructed for Eqn. 1 by appropriately discretizing the time derivative. In the current work, it’s desirable to utilize an unconditionally-stable, implicit scheme to allow a large timestep to be chosen based upon physical considerations rather than a potentially smaller stability-limited timestep. In the Cartesian embedded-boundary scheme, the cut-cell polyhedra can have arbitrarily small volumes, and a stability limit can be very restrictive. Using a large timestep also reduces the amount of computational work required to process the moving geometry and mesh through a complete simulation. In the current work, the backward Euler and 2nd-order backward time-integration schemes have both been utilized.

## 2.2.2 ALE formulation

Considering the motion of the rolling missile with dithering canards described in Sec. 2.1 in a body-fixed frame, the regions where relative motion occur are confined to a small area surrounding the canards. This is not unique to rotating airframes, and occurs in many applications such as rotorcraft or stage separation from space vehicles. It’s desirable to simulate the rotation of the entire missile using a rigid-body motion of the entire computational domain, and treat the relative motion of the canards separately within the rotating domain. This approach limits the amount of computational work that is required to process the moving geometry.

An Arbitrary-Lagrangian-Eulerian (ALE) formulation is utilized in order to account for the rigid-body motion of the computational domain (cf. Hirt et al. [22] for the development of the ALE formulation). This is accomplished by modifying the flux through a boundary to account for the motion of the boundary. For the inviscid flux vector utilized here, this becomes

$$\mathbf{f} \cdot \mathbf{n} = \begin{Bmatrix} \rho u_n \\ \rho u_n \mathbf{u} + p \mathbf{n} \\ \rho u_n e + p \mathbf{u} \cdot \mathbf{n} \end{Bmatrix} \quad (2)$$

where

$$u_n = (\mathbf{u} - \mathbf{u}_\Omega) \cdot \mathbf{n}$$

is the velocity relative to the moving boundary, and  $\mathbf{u}_\Omega$  is the velocity of the moving domain.

Hence the convective part of the flux is modified to account for the motion of the boundary, compared to the treatment for a fixed domain. A modified form of van Leer’s flux-vector splitting (FVS) [23] is used with the ALE formulation. This modification uses the Mach number relative to the moving boundary,  $M_{nc} = (\mathbf{u} - \mathbf{u}_\Omega) \cdot \mathbf{n}$ , when determining the characteristic speeds of the system.

Note that the geometry of the domain is expressed in the moving coordinate system, and must be transformed to the inertial system where the equations of motion are specified. While this does remove some of the algorithmic simplifications of a Cartesian scheme, it’s noted that the majority of faces of the computational domain have normals pointing in one of the Cartesian directions of the moving domain. These normals all transform identically and it’s possible to precompute and store this information at each timestep.

## 2.2.3 Relative motion

Figure 4 shows a schematic of a rigid-body moving through a fixed Cartesian mesh over one discrete timestep. The shaded region highlights cells which have been “swept” by the body through the timestep. These swept cells change volume and shape over the timestep, and can appear or disappear (or both) as well. The equations of motion for the deforming cells can be written in an integral conservation form as

$$\int_{V(t)} \mathbf{Q} dV = \left[ - \oint_{S(t)} \mathbf{f} \cdot \mathbf{n} dS \right] dt \quad (3)$$

Integrating Eqn. 3 using the backward Euler scheme gives

$$\frac{\mathbf{Q}^{n+1} - \frac{V^n}{V^{n+1}} \mathbf{Q}^n}{\Delta t} = - \frac{1}{V^{n+1}} \left[ \sum \mathbf{f} \cdot \mathbf{n} \Delta S \right]^{n+1} \quad (4)$$

This can be numerically integrated using the dual-time scheme outlined above. The term  $\frac{V^n}{V^{n+1}} \mathbf{Q}^n$  becomes a fixed source term in the dual-time scheme. However,  $\mathbf{Q}^n$  is only available on the mesh at time level  $n$ , while it is required on the mesh at time level  $n+1$  in order to integrate Eqn. 4. Rewriting Eqn. 4 gives

$$\frac{\mathbf{Q}^{n+1} - \hat{\mathbf{Q}}^n}{\Delta t} = - \frac{1}{V^{n+1}} \left[ \sum \mathbf{f} \cdot \mathbf{n} \Delta S \right]^{n+1} \quad (5)$$

where  $\hat{\mathbf{Q}}^n$  represents the state vector at time level  $n$  on the mesh at time level  $n+1$ .

In the current scheme, the vector  $\mathbf{Q}^n$  is “mapped” from the mesh at time level  $n$  to the new mesh at  $n+1$  using an interpolation operator  $I_n^{n+1}$ .

$$\hat{\mathbf{Q}}^n = I_n^{n+1} \mathbf{Q}^n \quad (6)$$



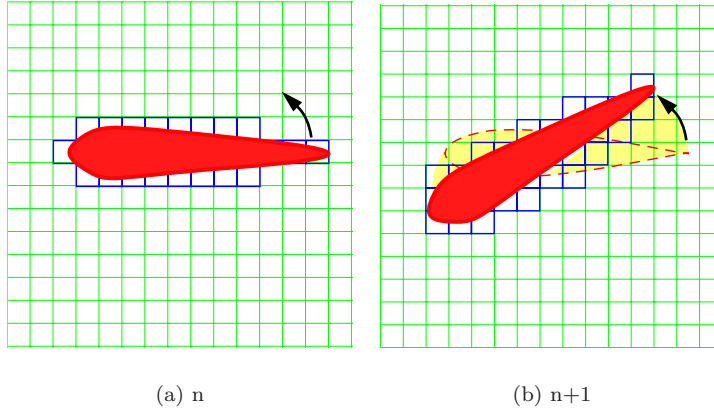


Figure 4: Schematic of a rigid-body moving through a Cartesian mesh.

If  $I_n^{n+1} = \frac{V^n}{V^{n+1}}$  then Eqn. 4 is satisfied. The interpolation operator  $I_n^{n+1}$  can be determined exactly using a space-time approach (cf. Refs. [24, 25]), however doing so in three dimensions poses a problem in 4-D mesh generation. Instead, an approximate scheme is desired which maintains conservation away from the region of the relative motion. The current scheme determines  $I_n^{n+1}$  exactly for all cells away from the moving boundary, as well as the majority of the cut cells at both time levels. For a small minority of the swept cells  $I_n^{n+1}$  is approximated. In the current work, the mapping of the solution between two meshes is processed external to the flow solver with a single-pass algorithm. Note that since the motion is prescribed, all of the meshes can be processed a priori, and in parallel.

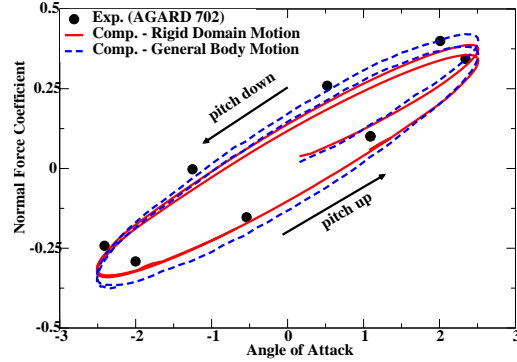


Figure 5: Time history of normal force coefficient. ( $M_\infty = 0.755$ ,  $\alpha(t) = 0.016 + 2.51 \sin(2\pi 62.5t)$ ).

### 3 Numerical Results

An oscillating NACA 0012 airfoil is used to examine the behavior of the approximate, relative-motion scheme outlined above. The transonic AGARD experimental test case [26] was computed using both the 2nd-order backward scheme with the conservative, moving-domain ALE scheme, and the 1st-order (in time) relative-motion scheme. Both schemes utilize the same spatially 2nd-order numerical flux formulation. The computed normal force variations with angle of attack are shown in Fig. 5. Both simulations capture the hysteresis caused by the unsteady shock formation, and are in relatively good agreement with the experimental data. Flow visualizations show no appreciable differences between the two simulations. Further analysis and validation of the numerical scheme will be presented in a future publication [17].

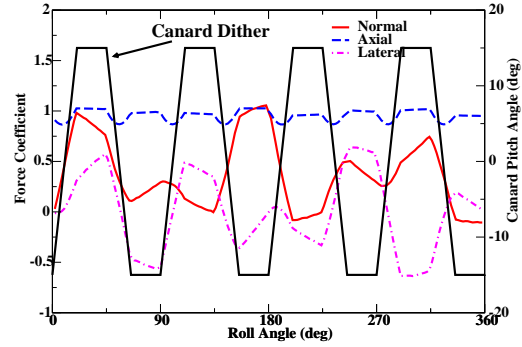
The general 3-D Cartesian scheme outlined above is utilized to simulate the rolling missile geometry with movable canards described in Sec. 2.1. These simulations are intended to both demonstrate the capabilities of the method, and examine several topics pertinent to the current application. The dynamic effects are examined by comparison with a series of static, steady-state simulations. The ability of the method as a predictive tool for rolling airframes is examined by comparison of the computed results with viscous simulations, and direct comparison with experimental data. Comparisons with experimental data are included for both the rolling airframe with dithering canards, and the prediction of dynamic stability derivatives.

### 3.1 Static-Roll Baselines

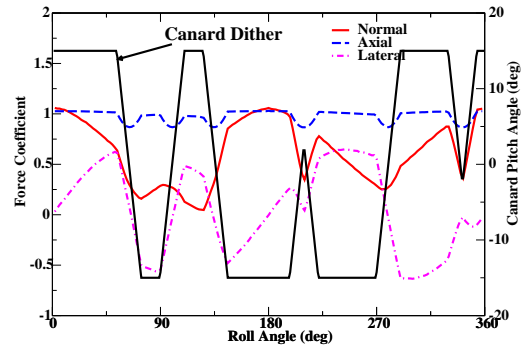
At the flow conditions of interest for the current work ( $M_\infty = 1.6$ ,  $\alpha = 3.0^\circ$ ), with the body rolling at 8.75Hz, a particle travels one body length in approximately 8 degrees of revolution (the non-dimensional roll-rate based on the freestream velocity and body diameter is  $St_D = 0.0087$ ). A particle in the canard vortex travels from the canard tip to the aft end of the body in approximately 6 degrees of body roll. This relatively low roll rate (and corresponding low vortex twist), implies that a series of static computations at different roll and canard orientations should be a good approximation for the true dynamic behavior. Given the lack of detailed experimental data,\* a series of “sequential-static” simulations of the current rolling/dithering missile were performed in order to have a baseline for comparison with the dynamic simulations.

Static, steady-state simulations were performed at 2 degree increments of roll using both Dither Schedules 0 and 1 from Fig. 2 to schedule the canard pitch angle. The computed forces for both sequential-static series of computations are summarized in Fig. 6. The axial force for both dither schedules remains relatively constant, and is effectively a function of the exposed frontal area of the canards. Both the lateral and normal forces show an immediate and strong response to changes in canard position. Note that in these static simulations a change in canard position is “felt” instantaneously by the tail section. In both dither schedules the normal and lateral forces change due to both roll orientation and canard pitch angle. For instance, in Dither Schedule 1 the normal force falls off while the lateral force increases as the body begins to roll. When the canards dither at  $\phi = 55^\circ$ , it has only a moderate effect on normal force as the canards are approaching vertical, however it causes the lateral force to immediately change sign. This is due to the canard lifting surfaces providing the majority of the lateral force in this roll orientation, as the canard vortices are located in a vertical plane. Similar analysis of the force response can be carried out for the entire roll/dither cycle.

While the details of the force and moment variations with roll angle provide insight, the main focus of the current work is to analyze the effect of the dynamics and canard dither on the roll-averaged loads. One method of analyzing the roll behavior of the missile is to examine the normal force and lateral force in a polar plot as the roll angle varies. These force polar plots are shown for the sequential-static simulations in Fig. 7. The radius of the plot is the magnitude of the crossflow force, and the polar angle is the roll angle. If the canards are fixed, then the force polar inscribes a circle as the body rotates, as the ca-



(a) Dither Schedule 0

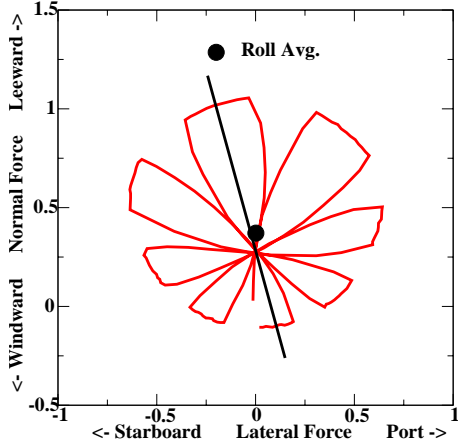


(b) Dither Schedule 1

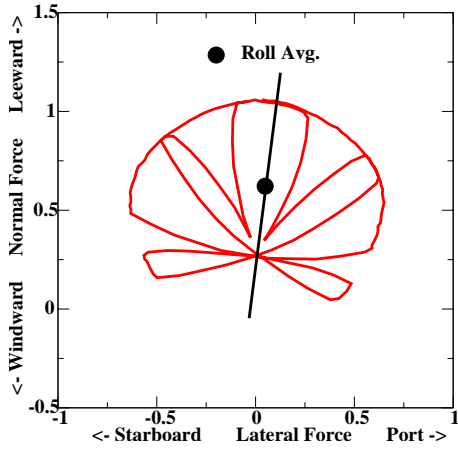
Figure 6: Computed forces for sequential-static roll simulations ( $M_\infty = 1.6$ ,  $\alpha = 3.0^\circ$ ,  $\dot{\phi} = 8.75\text{Hz}$ ).

nards continuously transition from providing normal force to lateral force and vice versa. A nearly identical plot can be generated by considering the pitching moment and yawing moment instead of normal and lateral forces. The dithering of the canards can be utilized to favor a particular region in the polar as the body rolls (relative to the circular plot for fixed canards). For example, Dither Schedule 0 is relatively balanced, while Dither Schedule 1 is almost a pure normal force (pitch) command. The bi-lateral symmetry of the plots is highlighted by including a solid line along the approximate axis of symmetry. The roll-averaged force lies on this axis of symmetry (see also Table 1).

\*The experimental data referred to in Sec. 3.2 and 3.3 was not available until recently.



(a) Dither Schedule 0



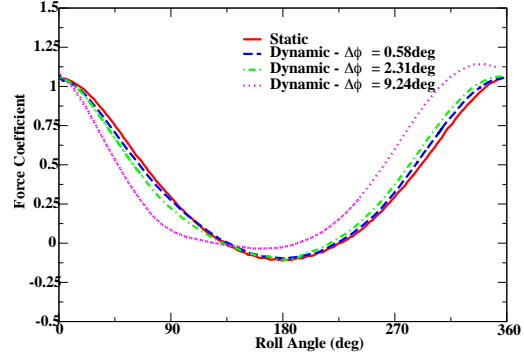
(b) Dither Schedule 1

Figure 7: Crossflow force polar for sequential-static roll simulations ( $M_\infty = 1.6$ ,  $\alpha = 3.0^\circ$ ,  $\dot{\phi} = 8.75\text{Hz}$ ).

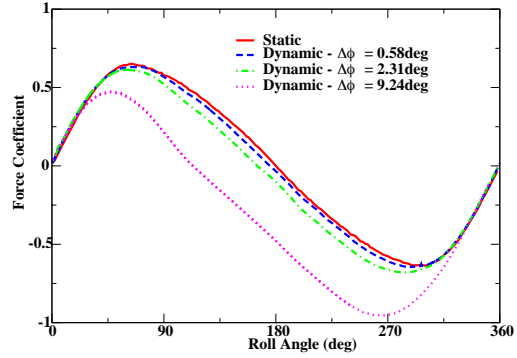
### 3.2 Dynamic Computations with Dithering Canards

With an unconditionally-stable implicit numerical scheme, such as is used in the current work, the timestep is limited by physical considerations and accuracy rather than stability. Due to this, an appropriate timestep must be determined for each unsteady simulation, much as an appropriate mesh resolution must be chosen for static simulations. One method for determining a timestep is to utilize a mesh which resolves all of the spatial scales of interest for the current problem, and perform a time resolution study using this mesh. The 3.4M cell mesh from the mesh res-

olution study described in Sec. 2.1 was utilized to compute a series of dynamic roll computations with the canards fixed at their maximum pitch angle ( $\delta_c = 15.0^\circ$ ). Three simulations with increasingly finer time resolutions were computed, along with a sequential-static simulation. The computed normal and lateral forces for this time resolution study are presented in Fig. 8. Since the canards are fixed, the force variation is sinusoidal, and should maintain nearly the same peak values as the sequential-static simulations, with a roughly  $6^\circ$  lag due to the body rotation at this roll rate. It's seen that this is provided by the finest timestep computed,  $\Delta t = 0.58^\circ$  of roll. As a compromise between accuracy and efficiency, a timestep of  $\Delta t = 1.0^\circ$  of roll was utilized for all subsequent computations.



(a) Normal Force



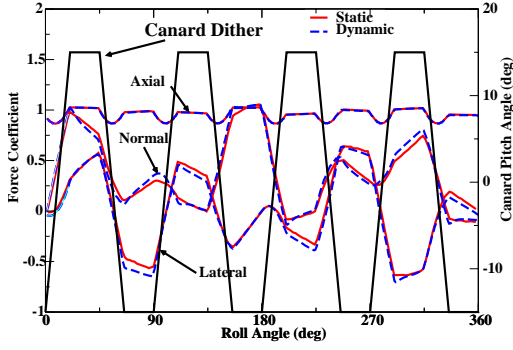
(b) Lateral Force

Figure 8: Time resolution study with fixed canards ( $M_\infty = 1.6$ ,  $\alpha = 3.0^\circ$ ,  $\dot{\phi} = 8.75\text{Hz}$ ,  $\delta_c = 15.0^\circ$ ).

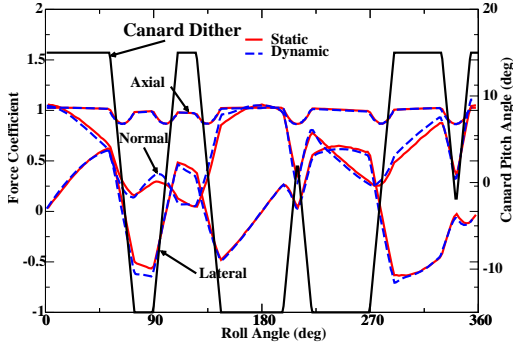
In order to examine the dynamic effects for the rolling airframe, the dither schedules presented in Fig. 2 were computed using the Cartesian general moving boundary scheme outlined in Sec. 2.2.



The force variation for both dither schedules is compared to the sequential-static simulations in Fig. 9. The agreement between the static and dynamic simulations is very close, as anticipated. Whenever the canards abruptly stop their motion, the fluid cannot respond instantaneously to the rigid structural motion, and hence the dynamic simulations “overshoot” the static simulations. An example of this is seen near  $\phi = 22^\circ$  for Dither Schedule 0. The dynamic simulation predicts slightly more normal force at the end of the canard dither motion, and then under-predicts after the motion has stopped. This behavior is similar to the hysteresis seen in Fig. 5 for the oscillating airfoil. The predicted roll-averaged quantities are summarized in Table 1. There is close agreement between the static and dynamic roll-averaged normal and axial forces, and somewhat larger percentage differences in the lateral forces.



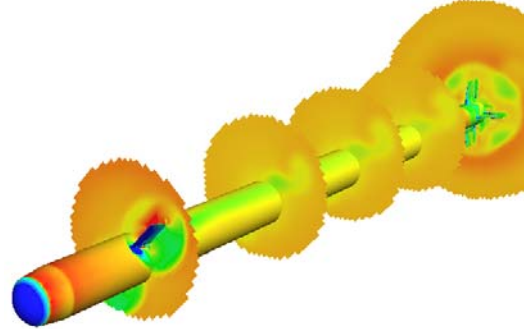
(a) Dither Schedule 0



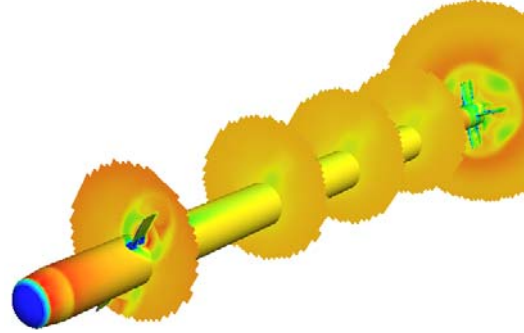
(b) Dither Schedule 1

Figure 9: Comparison of static and dynamic force variation ( $M_\infty = 1.6$ ,  $\alpha = 3.0^\circ$ ,  $\dot{\phi} = 8.75\text{Hz}$ ).

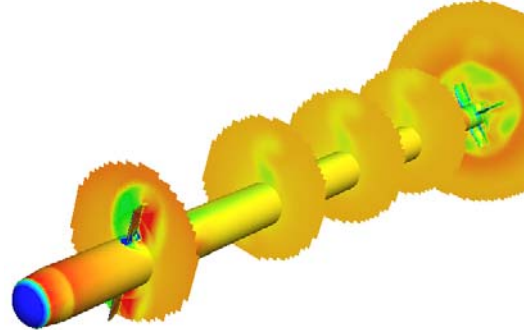
Figure 10 shows snapshots of velocity magnitude cutting planes (blue is low, red is high) from the dynamic simulation for Dither Schedule 0.



(a)  $\phi = 45.5^\circ$



(b)  $\phi = 57.6^\circ$



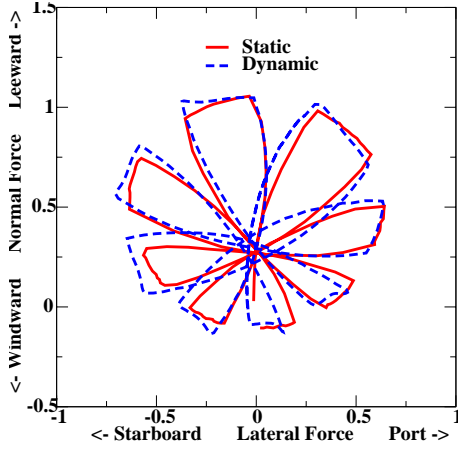
(c)  $\phi = 71.8^\circ$

Figure 10: Velocity magnitude contours for Dither Schedule 0 ( $M_\infty = 1.6$ ,  $\alpha = 3.0^\circ$ ,  $\dot{\phi} = 8.75\text{Hz}$ ).

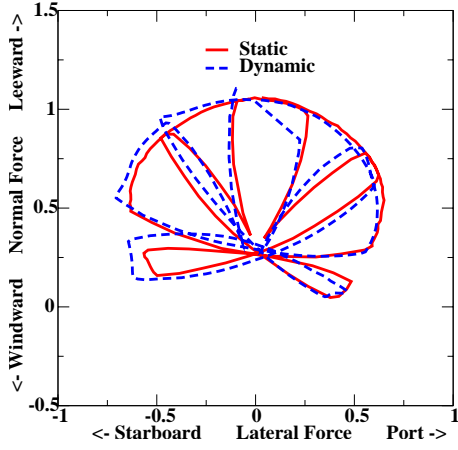
These show that the canard vortices convect back to the exit plane of the computational domain aft of the tail fins. At this angle of attack, there is a strong interaction between the canard vortices and the tail fins. The canard tip vortex can be seen just outside the tail fin bow shock in the last

axial cutting plane on the body. The twist of the canard vortices is evident, though difficult to discern at this low body roll rate. The change in the shock structure on the canards as they dither can be seen, as well as the change in sense of rotation of the canard tip vortices.

Force polar comparisons of the static and dynamic simulations for both dither schedules are presented in Fig. 11. The effect of the dynamics can be seen as enlarging the areas of the “leaves” of the rosettes, as compared to the static simulations. The roll rate changes the sweep of the leaf, while the canard motion changes the outer limit.



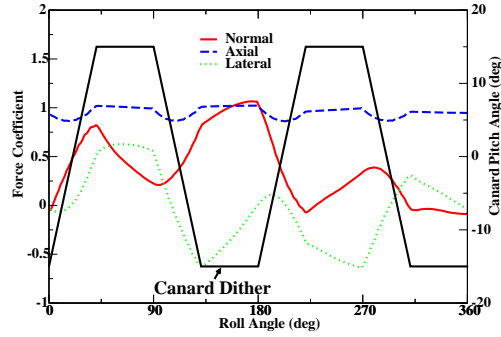
(a) Dither Schedule 0



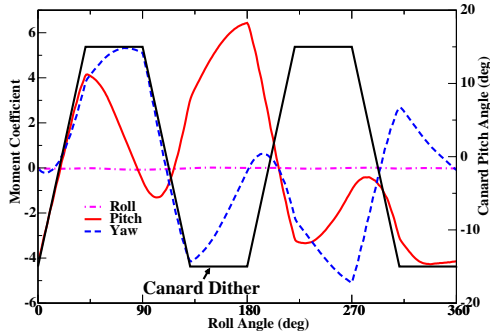
(b) Dither Schedule 1

Figure 11: Comparison of static and dynamic force polars ( $M_\infty = 1.6$ ,  $\alpha = 3.0^\circ$ ,  $\dot{\phi} = 8.75\text{Hz}$ ).

As noted in the comparison of the static and dynamic simulations above, the dynamic effects with the body rolling at  $8.75\text{Hz}$  are not substantial. In order to assess the dynamic effects at higher roll rates, a simulation was performed using a roll rate of  $17.5\text{Hz}$  and Dither Schedule 0. Note that at this higher roll rate, the canards dither half as frequently as shown in Fig. 2. The dither schedule for this higher roll rate is included in the summary force and moment plots in Fig. 12. It's seen that while the higher roll rate produces a different variation of the forces and moments with roll angle, the roll-averaged values are nearly unchanged (cf. Table 1). The roll-averaged rolling-moment does decrease at the higher roll rate due to the cant of the tail fins. The yawing moment also increases in magnitude, as the aft end of the body lags the canards at the higher roll rate. The effects of roll rate will be discussed further in the next section on dynamic derivatives. A comparison of the force polars for the  $8.75\text{Hz}$  and  $17.5\text{Hz}$  roll rates is presented in Fig. 13. The two paths are different, but both are relatively balanced and provide the same mean forces.



(a) Forces



(b) Moments

Figure 12: Dynamic load variation ( $M_\infty = 1.6$ ,  $\alpha = 3.0^\circ$ ,  $\dot{\phi} = 17.5\text{Hz}$ ).

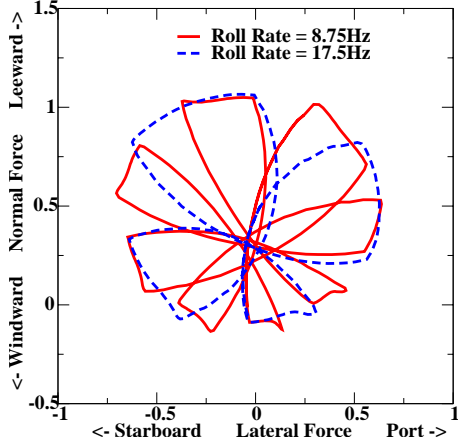
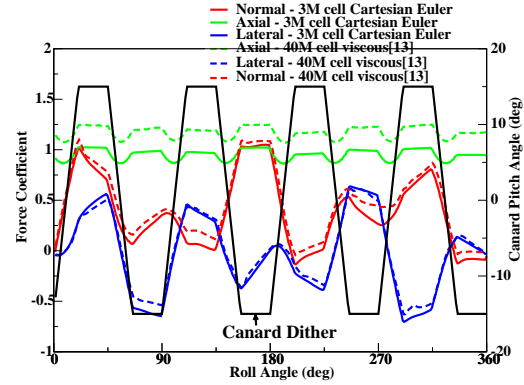


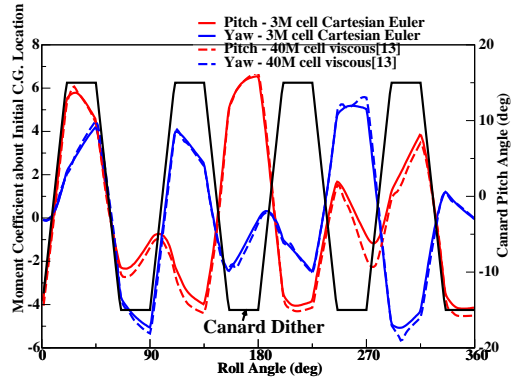
Figure 13: Comparison of dynamic force polars ( $M_\infty = 1.6$ ,  $\alpha = 3.0^\circ$ ).

A viscous, high-resolution (40M cells, 12000 timesteps/rev) reference simulation by Nygaard and Meakin [13] is utilized as a baseline for comparison with the current inviscid results. The computed forces and moments for the simulation using Dither Schedule 0 are compared to the viscous simulations in Fig. 14. The agreement between the two simulations is very good throughout the roll cycle. As expected, there is a constant increment in axial force between the current inviscid results and the viscous simulations due to wall shear stress. The viscous results do consistently predict a slightly higher normal force through the roll cycle, and a slightly lower (more nose down) pitching moment compared to the current results.

In order to assess the predictive capability of the current approach, a simulation of a recent experimental test [14] was performed. The experiment included both the ability to roll the airframe and dither the canards, and also provided a measure of the experimental uncertainty. The actual canard motion from the experiment over ten revolutions is presented in Fig. 15, along with an ensemble of averages of the canard position, and an analytic approximation to the ensemble average which is used to schedule the canards in the simulation. Again, the canard dither motion is periodic over a single body revolution. The computed forces and moments using this dither motion are presented in Fig. 16. The forces and moments again show an immediate and strong response to the motion of the canards. As opposed to the previous dither computations, this dither motion produces a yaw of the body. This can be clearly seen in the force polar (Fig. 17). The roll-averaged forces and moments are compared against the experimental values in Table 2. In all cases, the computed values are within the experimental uncertainty.



(a) Forces



(b) Moments

Figure 14: Comparison of Dither Schedule 0 load histories with viscous results from [13] ( $M_\infty = 1.6$ ,  $\alpha = 3.0^\circ$ ,  $\dot{\phi} = 8.75\text{Hz}$ ).

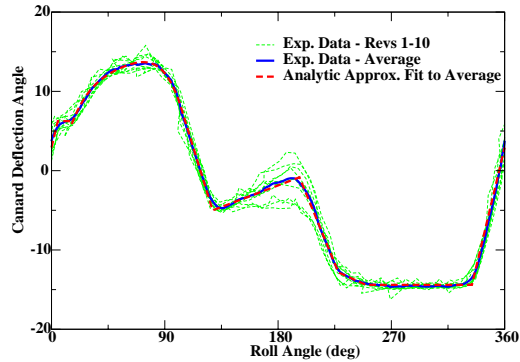


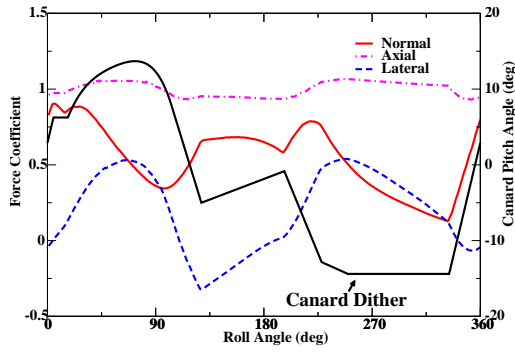
Figure 15: Experimental canard motion [14] ( $M_\infty = 1.6$ ,  $\alpha = 3.0^\circ$ ,  $\dot{\phi} = 18\text{Hz}$ ).

Case	$C_A$	$C_N$	$C_Y$	$C_l$	$C_m$	$C_n$
Static, 8.75Hz, Sched. 0	0.95	0.37	0.0015	N/A	N/A	N/A
Dynamic, 8.75Hz, Sched. 0	0.95	0.38	-0.035	0.013	0.18	-0.011
Dynamic, 17.5Hz, Sched. 0	0.95	0.38	-0.035	-0.020	0.19	-0.25
Static, 8.75Hz, Sched. 1	0.97	0.62	0.049	N/A	N/A	N/A
Dynamic, 8.75Hz, Sched. 1	0.97	0.62	0.026	0.013	2.5	0.38

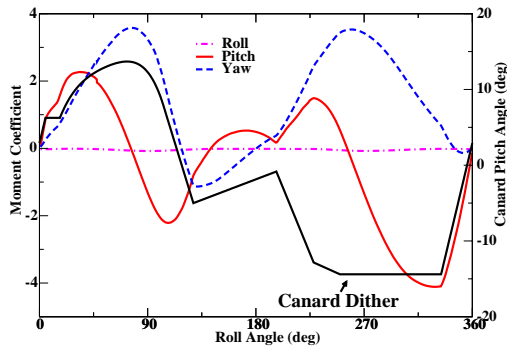
Table 1: Roll-averaged forces and moments for Dither Schedules 0 and 1 ( $M_\infty = 1.6$ ,  $\alpha = 3.0^\circ$ ).

	$C_N$	$C_Y$	$C_l$	$C_m$	$C_n$
Experiment [14]	0.45 – 0.61	0.15 – 0.20	-0.036 – -0.019	-1.5 – -0.40	0.93 – 1.5
Computed	0.55	0.20	-0.034	-0.48	1.46

Table 2: Roll-averaged forces and moments for Fig. 15 dither schedule ( $M_\infty = 1.6$ ,  $\alpha = 3.0^\circ$ ,  $\dot{\phi} = 18\text{Hz}$ ).



(a) Forces



(b) Moments

Figure 16: Dynamic load variation for Fig. 15 dither schedule ( $M_\infty = 1.6$ ,  $\alpha = 3.0^\circ$ ,  $\dot{\phi} = 18.0\text{Hz}$ ).

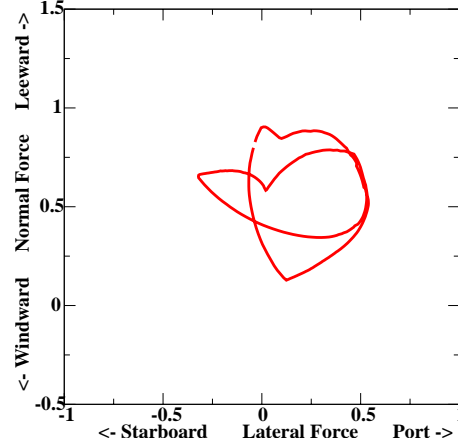


Figure 17: Dynamic force polar for Fig. 15 dither schedule ( $M_\infty = 1.6$ ,  $\alpha = 3.0^\circ$ ,  $\dot{\phi} = 18.0\text{Hz}$ ).

### 3.3 Dynamic Derivatives with Fixed Canards

The previous sections simulate the actual motion of the rolling missile with dithering canards. Rather than simulate the actual motion for each dynamic case of interest, it's preferable to build a computational database which is capable of simulating any dynamic motion. One common method of building a computational database is to perform a parametric study for all of the possible geometric configurations and freestream conditions using a static, steady-state flow solver. This approach can be extended to include dynamic effects by performing a similar parametric study, varying the relevant dynamic parameters such as body roll rate (cf. Refs. [27, 9]). From this dynamic parameter study, dynamic stability derivatives can be computed and used with the static derivatives to build a computational database. This approach is especially relevant to missile configurations, which are highly-maneuverable (e.g.  $\pm 15g$ ), and hence frequently encounter an extreme range of flow conditions which require the higher-order dynamic derivatives.

Simulations of the rolling missile with the canards fixed in the zero-deflection position were performed at three roll rates to match the available experimental data [14]; 9Hz, 12Hz, and 18Hz. For the current configuration, the quantities of primary interest for dynamic modeling are the roll- and yaw-damping,

$$C_{l_p} = \frac{2V_\infty}{D} \frac{\partial C_l}{\partial p} \quad C_{n_p} = \frac{2V_\infty}{D} \frac{\partial C_n}{\partial p} \quad (7)$$

The pitching moment remains essentially constant at the roll rates and angle of attack being investigated here. Figure 18 presents the yaw- and roll-damping against the experimental data. The agreement with the experimental data is very good, and all of the computed data points are within the experimental uncertainty. At these relatively low roll rates, both the yawing and rolling moments show a linear dependence on roll rate. The damping coefficients hence correspond to the slopes of the curves in Fig. 18. As the roll rate is increased, the canard vortices experience more twist as they travel the length of the body. This increase in twist causes the yawing moment relative to the c.g. location to increase as the roll rate increases, as the flow on the aft end increasingly lags behind the canards. The rolling moment is most strongly influenced by the cant of the tail fins. At these flow conditions, both the computations and experiment show that if the missile were unconstrained, the fins would cause it to roll at 10-15Hz.

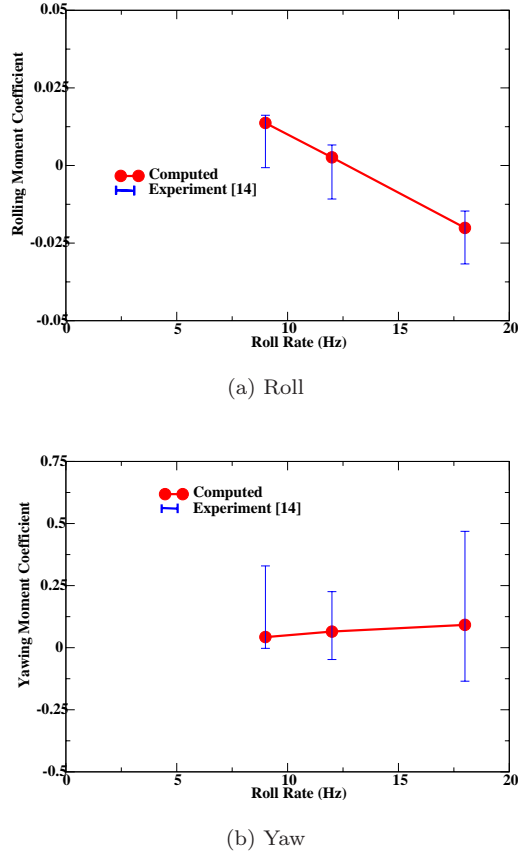


Figure 18: Dynamic derivatives with fixed canards ( $M_\infty = 1.6$ ,  $\alpha = 3.0^\circ$ ,  $\delta_c = 0.0^\circ$ ).

## 4 Summary

A 3-D Cartesian method for simulating the general prescribed motion of rigid bodies was developed and applied to the analysis of a rolling airframe with movable canard control surfaces. Dynamic simulations for several canard dither schedules and roll rates were performed, and compared against static simulations, high-resolution viscous simulations, and relevant experimental data. The results show that the current scheme can be used as an effective predictive tool for both the complete rolling motion with canard dither, as well as for computing dynamic stability derivatives. At the relatively low roll rates considered in this work, a series of static, steady-state simulations provides a good approximation to the actual dynamic motion. Comparisons with the viscous results of Nygaard and Meakin [13] show that the current inviscid results capture the same trends, and can be corrected with a constant viscous axial force increment. Direct comparison with recent experimental data



shows that the computed forces and moments are within the experimental uncertainty for all simulations considered.

## 5 Acknowledgments

The authors would like to thank Dr. Tor Nygaard of ELORET and Dr. Robert Meakin of the U.S. Army AFDD for providing the viscous simulation results for comparison.

## References

- [1] Aftosmis, M.J., Berger, M.J., and Melton, J.E., "Robust and Efficient Cartesian Mesh Generation for Component-Based Geometry," *AIAA Journal*, vol. 36, pp. 952–960, June 1998.
- [2] Aftosmis, M.J., Berger, M.J., and Adomavicius, G., "A Parallel Multilevel Method for Adaptively Refined Cartesian Grids with Embedded Boundaries," AIAA Paper 2000-0808, Jan. 2000.
- [3] Meakin, R.L. and Suhs, N., "Unsteady Aerodynamic Simulation of Multiple Bodies in Relative Motion," AIAA Paper 89-1996-CP, June 1989.
- [4] Batina, J., "Unsteady Euler Algorithm with Unstructured Dynamic Mesh for Complex Aircraft Aeroelastic Analysis," AIAA Paper 89-1189, June 1989.
- [5] Löhner, R., "Adaptive Remeshing for Transient Problems," *Computer Methods in Applied Mechanics and Engineering*, vol. 75, pp. 195–214, 1989.
- [6] Venkatakrishnan, V. and Mavriplis, D. J., "Computation of Unsteady Flows over Complex Geometries in Relative Motion," in *1st AFOSR Conference on Dynamic Motion CFD*, June 1996.
- [7] Weinacht, P., Sturek, W.B., and Schiff, L.B., "Navier-Stokes Predictions of Pitch-Damping for Axisymmetric Shell Using Steady Coning Motion," AIAA Paper 91-2855, Aug. 1991.
- [8] Weinacht, P., "Navier-Stokes Predictions of the Individual Components of the Pitch-Damping Sum," *Journal of Spacecraft and Rockets*, vol. 35, pp. 598–605, Oct. 1998.
- [9] Oktay, E. and Akay, H. U., "CFD Predictions of Dynamic Derivatives for Missiles," AIAA Paper 2002-0276, Jan. 2002.
- [10] Park, S.H., Kim, Y., and Kwon, J.H., "Prediction of Dynamic Damping Coefficients Using Unsteady Dual-Time Stepping Method," AIAA Paper 2002-0715, Jan. 2002.
- [11] Janus, J.M., Whitfield, D.L., Horstman, H.Z., and Mansfield, F., "Computation of the Unsteady Flowfield About a Counter-rotating Prop-Fan Cruise Missile," AIAA Paper 90-3093-CP, Aug. 1990.
- [12] Hall, L.H., "Rolling Airframe Missile Aerodynamic Predictions Using a Chimera Approach for Dithering Canards," AIAA Paper 2002-0405, Jan. 2002.
- [13] Nygaard, T. and Meakin, R., "An Aerodynamic Analysis of a Spinning Missile with Dithering Canards," AIAA Paper 2002-2799, June 2002.
- [14] "Defensive Missile Wind Tunnel Test for the Validation and Verification of CFD Codes," Dynetics Technical Report, Jan. 2002.
- [15] Stalnaker, J. private communication, Oct. 1999.
- [16] Aftosmis, M.J., "Solution Adaptive Cartesian Grid Methods for Aerodynamic Flows with Complex Geometries," VKI Lecture Series 97-02, Mar. 1997.
- [17] Murman, S.M., Aftosmis, M.J., and Berger, M.J., "A 3-D Time-Dependent Cartesian Method with Moving Boundaries," submitted for presentation at the AIAA Aerosciences Meeting, Reno, NV., Jan. 2003.
- [18] Merkle, C.L. and Athavale, M., "A Time Accurate Unsteady Incompressible Algorithm Based on Artificial Compressibility," AIAA Paper 87-1137, June 1987.
- [19] Rogers, S.E., Kwak, D., and Kiris, C., "Numerical Solution of the Incompressible Navier-Stokes Equations for Steady and Time-Dependent Problems," *AIAA Journal*, vol. 29, no. 4, pp. 603–610, 1991.
- [20] Jameson, A., "Time Dependent Calculations Using Multigrid with Applications to Unsteady Flows Past Airfoils," AIAA Paper 91-1596, June 1991.
- [21] Melson, N.D., Sanetrik, M.D., and Atkins, H.L., "Time-accurate Navier-Stokes Calculations with Multigrid Acceleration," in *Proceedings of the Sixth Copper Mountain Conference on Multigrid Methods*, Apr. 1993.
- [22] Hirt, C.W., Amsden, A.A., and Cook, J.L., "An Arbitrary Lagrangian-Eulerian Computing Method for All Flow Speeds," *Journal of Computational Physics*, vol. 14, pp. 227–253, 1974.

- [23] van Leer, B., “Flux-Vector Splitting for the Euler Equations,” in *Lecture Notes in Physics*, vol. 170, pp. 507–512, Springer Verlag, Berlin, 1982.
- [24] Zhang, H., Reggio, M., Trépanier, J.Y., and Camarero, R., “Discrete Form of the GCL for Moving Meshes and its Implementation in CFD Schemes,” *Computers in Fluids*, vol. 22, no. 1, pp. 9–23, 1993.
- [25] Lesoinne, M. and Farhat, C., “Geometric Conservation Laws for Flow Problems with Moving Boundaries and Deformable Meshes, and Their Impact on Aeroelastic Computations,” *Computer Methods in Applied Mechanics and Engineering*, vol. 134, pp. 71–90, 1996.
- [26] Landon, R.H., “Compendium of Unsteady Aerodynamic Measurements,” AGARD Report No. 702, Aug. 1982.
- [27] Park, M. A. and Green, L. L., “Steady-state Computation of Constant Rotational Rate Dynamic Stability Derivatives,” AIAA Paper 2000-4321, June 2000.